UC San Diego

UC San Diego Previously Published Works

Title

Discrimination of Breast Cancer from Healthy Breast Tissue Using a Three-component Diffusion-weighted MRI Model

Permalink

https://escholarship.org/uc/item/5f84x9xr

Journal

Clinical Cancer Research, 27(4)

ISSN

1078-0432

Authors

Andreassen, Maren M Sjaastad
Rodríguez-Soto, Ana E
Conlin, Christopher C
et al.

Publication Date

2021-02-15

DOI

10.1158/1078-0432.ccr-20-2017

Peer reviewed

eScholarship.org Powered by the California Digital Library
University of California

Published OnlineFirst November 4, 2020; DOI: 10.1158/1078-0432.CCR-20-2017

Discrimination of Breast Cancer from Healthy Breast Tissue Using a Three-component Diffusion-weighted MRI Model

Maren M. Sjaastad Andreassen[1], Ana E. Rodríguez-Soto[2], Christopher C. Conlin[2], Igor Vidić[8], Tyler M. Seibert[2,4,5], Anne M. Wallace[6], Somaye Zare[3], Joshua Kuperman[2], Boya Abudu[7], Grace S. Ahn[7], Michael Hahn[2], Neil P. Jerome[1,8], Agnes Østlie[1], Tone F. Bathen[1,9], Haydee Ojeda-Fournier[2], Pål Erik Goa[8,9], Rebecca Rakow-Penner[2], and Anders M. Dale[2,10]

ABSTRACT

Purpose: Diffusion-weighted MRI (DW-MRI) is a contrast-free modality that has demonstrated ability to discriminate between predefined benign and malignant breast lesions. However, how well DW-MRI discriminates cancer from all other breast tissue voxels in a clinical setting is unknown. Here we explore the voxelwise ability to distinguish cancer from healthy breast tissue using signal contributions from the newly developed three-component multi-b-value DW-MRI model.

Experimental Design: Patients with pathology-proven breast cancer from two datasets ($n = 81$ and $n = 25$) underwent multi-b-value DW-MRI. The three-component signal contributions C_1 and C_2 and their product, C_1C_2, and signal fractions F_1, F_2, and F_1F_2 were compared with the image defined on maximum b-value (DWI_{max}), conventional apparent diffusion coefficient (ADC), and apparent diffusion kurtosis (K_{app}). The ability to discriminate between cancer and healthy breast tissue was assessed by the false-positive rate given a sensitivity of 80% (FPR_{80}) and ROC AUC.

Results: Mean FPR_{80} for both datasets was 0.016 [95% confidence interval (CI), 0.008–0.024] for C_1C_2, 0.136 (95% CI, 0.092–0.180) for C_1, 0.068 (95% CI, 0.049–0.087) for C_2, 0.462 (95% CI, 0.425–0.499) for F_1F_2, 0.832 (95% CI, 0.797–0.868) for F_1, 0.176 (95% CI, 0.150–0.203) for F_2, 0.159 (95% CI, 0.114–0.204) for DWI_{max}, 0.731 (95% CI, 0.692–0.770) for ADC, and 0.684 (95% CI, 0.660–0.709) for K_{app}. Mean ROC AUC for C_1C_2 was 0.984 (95% CI, 0.977–0.991).

Conclusions: The C_1C_2 parameter of the three-component model yields a clinically useful discrimination between cancer and healthy breast tissue, superior to other DW-MRI methods and obliviating predefining lesions. This novel DW-MRI method may serve as noncontrast alternative to standard-of-care dynamic contrast-enhanced MRI.

Introduction

Numerous studies have indicated that early breast cancer detection, with dynamic contrast-enhanced MRI (DCE-MRI), has higher sensitivity than current screening programs (ultrasound and mammography; refs. 1–5). However, DCE–MRI has a number of limitations such as conflicting results regarding specificity (2–6), dependency on expert radiologist readers, additional scan time and costs, and the use of gadolinium-based contrast agents that are linked to deposition in the brain (7). In contrast, diffusion-weighted MRI (DW-MRI) does not require exogenous contrast and yields quantitative information of tissue microstructure by detecting diffusion of water molecules through application of varying degree of diffusion weighting.

Various diffusion models have demonstrated comparable ability to DCE-MRI in discriminating between *predefined* benign and malignant lesions in small regions of interest (ROI) in the breast (8–14). However, DW-MRI would increase its clinical utility and practicality in breast cancer screening, treatment evaluation, surgical planning, and surveillance if it could also discriminate cancer from all healthy breast tissue, not relying on lesions being predefined by radiologists. DW-MRI of healthy breast tissue is problematic because it consists of varying degree of admixtures of fatty and fibroglandular tissue (15) which creates an intravoxel fatty component on DW-MRI (16). Fatty tissue is primarily made up of adipocytes which contain a large lipid droplet that occupies >90% of the cell volume, leaving only a small rim of water-containing cytoplasm. Common fat suppression techniques are designed to

[1]Department of Circulation and Medical Imaging, Norwegian University of Science and Technology, Trondheim, Norway. [2]Department of Radiology, University of California San Diego, La Jolla, California. [3]Department of Pathology, University of California San Diego, La Jolla, California. [4]Department of Radiation Medicine and Applied Sciences, University of California San Diego, La Jolla, California. [5]Department of Bioengineering, University of California San Diego, La Jolla, California. [6]Department of Surgery, University of California San Diego, La Jolla, California. [7]School of Medicine, University of California San Diego, La Jolla, California. [8]Department of Physics, Norwegian University of Science and Technology, Trondheim, Norway. [9]Department of Radiology and Nuclear Medicine, St. Olav's University Hospital, Trondheim, Norway. [10]Department of Neuroscience, University of California San Diego, La Jolla, California.

Note: Supplementary data for this article are available at Clinical Cancer Research Online (http://clincancerres.aacrjournals.org/).

M.M.S. Andreassen and A.E. Rodríguez-Soto contributed equally as co-first authors of this article.

R. Rakow-Penner and A.M. Dale contributed equally as co-last authors of this article.

Corresponding Author: Rebecca Rakow-Penner, 9400 Campus Point Drive #7316, La Jolla, CA 92093. Phone: 858-534-8259; Fax: 858-534-1078; E-mail: rrakowpenner@health.ucsd.edu

Clin Cancer Res 2021;27:1094–104

doi: 10.1158/1078-0432.CCR-20-2017

©2020 American Association for Cancer Research.

Downloaded from clincancerres.aacrjournals.org on October 19, 2021. © 2021 American Association for Cancer Research.

Published OnlineFirst November 4, 2020; DOI: 10.1158/1078-0432.CCR-20-2017

Translational Relevance

Here we present a novel methodology to discriminate cancer from surrounding healthy breast tissue. We employ an advanced diffusion-weighted MRI (DW-MRI) model without the use of a contrast agent and find highly promising diagnostic properties of the derived parameter C_1C_2. The results indicate that C_1C_2 may serve as a noncontrast alternative to standard-of-care dynamic contrast-enhanced MRI, which removes the need to administer gadolinium contrast, decreasing costs and any accumulation of gadolinium in the brain. Further clinical utility of C_1C_2 is reflected by accounting for admixed fatty tissue in healthy breast tissue and obliviation of predefined lesions that conventional quantitative DW-MRI metrics use. Thus, C_1C_2 may yield increased clinical utility and practicality in breast cancer evaluation, where lesions are not predefined. Furthermore, the diagnostic properties were generalized across sites, scanners, and acquisition protocols, which is important for feasibility of large-scale studies for validation in routine breast cancer detection and follow-up.

suppress the lipid component (17). However, studies have reported highly restricted diffusion in fat-suppressed healthy breast tissue (18, 19), which suggests that the water component in fatty tissue remains on conventional DW-MRI. The restricted water component in fatty tissue is especially problematic because it confounds the slow diffusion signal from intracellular cancer tissue. Thus, advanced imaging techniques are needed to discriminate cancer from all healthy breast tissue on a voxelwise level including the restricted water component in the intravoxel fatty tissue.

Advanced, multicomponent partial volume models that use extended ranges of *b*-values (typically up to 2,000–3,000 seconds/mm^2) may theoretically isolate the slowly diffusing water pool present in cancer tissue and have become an emerging standard in several imaging domains (20–26). Here, the DW-MRI signal is modeled as a combination of exponential decays with corresponding component apparent diffusion coefficients (*ADCs*), where the weighting of each component represents the attribution from a distinct pool of water from the total diffusion signal. Furthermore, selected multicomponent partial volume models, such as restriction spectrum imaging (RSI; refs. 24–26), use tissue-specific, predetermined component *ADCs* which ensures linearization of the model, comparability across patients, and rapid fitting of diffusion signal which is essential for clinical application. This is fundamentally different from conventional approaches where *ADCs* are not fixed but are left free and determined for each voxel independently. However, these methods are not yet well investigated in the breast.

Initial results of multicomponent partial volume models in the breast have been demonstrated by Vidić and colleagues (12), showing that the normalized magnitude of the slowest component in a two-component model was excellent (AUC = 0.99) in discriminating between *predefined* benign and malignant breast lesions. Building on these findings, the multicomponent model was optimized to fit the DW-MRI signal across all voxels in all breast tissue, including cancer and healthy breast tissue, resulting in a three-component model with empirical *ADCs* globally determined across patients, scanners, and sites (19). The three-component model was able to explain all voxels in all breast tissue, including the restricted water component in fatty tissue, rather than the averaged signal of an ROI (27–29).

The main objective of this study is to explore the ability of estimates derived from a three-component model to discriminate breast cancer from healthy breast tissue and to compare it with other DW-MRI methods.

Materials and Methods

Patients

To validate the discriminatory power of the three-component model across scanners and sites, two datasets of patients with pathology-proven breast cancer from a U.S. site (n = 81) and a European site (n = 25) were included (**Table 1**). Note that 49 cases from the U.S. site and all cases from the European site were also used to determine the three-component model with fixed *ADCs* for breast tissue (19). In addition, cases from the European site have been previously used for DW-MRI modeling of previously defined benign and malignant lesions (12, 30–33), linking DW-MRI signal to histologic specimen (34) and distortion correction techniques (35). Written informed consent was obtained from patients at both sites and the studies were conducted in accordance with the Declaration of Helsinki.

U.S. dataset

Ninety-five patients with pathology-proven breast cancer with no cytotoxic regimens, chemotherapy, or ipsilateral radiotherapy for this malignancy prior to MRI scanning were eligible for this retrospective study. The study was approved by the Institutional Review Board of the U.S. site. Patients included for evaluation were imaged between December 2015 and ended in June 2019. Tumor categorization was done by histopathologic analysis of core needle and open incisional biopsies. In total, 14 patients were excluded from the study; nine patients had contralateral cancer or mastectomy, one patient had no visible cancer tissue on DW-MRI, and in four patients image quality was low [low signal-to-noise ratio (n = 2), poor fat saturation (n = 1), and severe image distortion (n = 1)], resulting in 81 patients.

European dataset

This prospective study was approved by the Regional Committees for Medical and Health Research Ethics (REC Central Norway, 2011/568). The recruitment of patients began in August 2014 and ended in August 2016. Twenty-five patients with pathology-proven breast cancer with inclusion criteria and tumor categorization similar to that of the U.S. site were included; for more details, see inclusion of malignant lesions from Vidić and colleagues (12).

MRI acquisition

MRI data were acquired on a 3T GE scanner (MR750, DV25–26, GE Healthcare) and an eight-channel breast array coil with a bilateral axial imaging plane for the U.S. dataset, while patients from the European dataset were imaged with a 3T Siemens scanner (Skyra, VD13-E11, Siemens Healthcare) and a 16-channel breast array coil with a unilateral sagittal imaging plane. Differences in scanner and pulse sequence parameters across sites were used to determine that the discriminatory potential of the three-component model is robust for data collected in different scanners and pulse sequence parameters. In addition to gadolinium DCE-MRI and T2 images, both datasets included high *b*-value DW-MRI acquisition:

U.S. dataset protocol

Bilateral axial DW-MRI was performed using reduced field of view (FOV) echo-planar imaging (EPI) including the following parameters:

Downloaded from clincancerres.aacrjournals.org on October 19, 2021. © 2021 American Association for Cancer Research.

Published OnlineFirst November 4, 2020; DOI: 10.1158/1078-0432.CCR-20-2017

Table 1. Table of patient characteristics. ER (estrogen receptor) and PR (progesterone receptor) status were assessed by IHC and was considered positive if ≥1% stained nuclei was present in 10 high-power fields (50). HER2 status was assessed by IHC and FISH according to ASCO/CAP guidelines 2013 (51) or 2018 (ref. 52; depending on time of recruitment); positivity was defined as an IHC score of 3+, or 2+ with a gene to chromosome ratio ≥ 2.0 by FISH.

	U.S. dataset	European dataset
No. of patients	81	25
Median patient age, years (range)	51 (20–84)	53 (29–75)
Mean tumor volume, cm^3 (range)	13.1 (0.2–105.9)	2.5 (0.5–5.8)
Histologic type		
Invasive carcinoma of no special type	64	17
Invasive lobular carcinoma	6	1
Tubular carcinoma	0	1
Mucinous carcinoma	0	1
Carcinoma with medullary features	0	3
Metaplastic carcinoma of no special type	4	0
Invasive papillary carcinoma	0	1
Mixed invasive carcinoma of no special type and invasive lobular carcinoma	3	0
Mixed invasive carcinoma of no special type and mucinous carcinoma	1	0
Ductal carcinoma *in situ*	3	1
Histologic grade		
1	3	5
2	28	9
2/3	0	1
3	47	8
Not analyzed	3	2
ER status		
Positive	53	23
Negative	27	1
Not analyzed	1	1
PR status		
Positive	50	20
Negative	30	4
Not analyzed	1	1
HER2 status		
Positive	14	7
Negative	64	17
Not analyzed	3	1
Lesion type		
Mass	67	25
NME	13	0
Mass and NME	1	0

Abbreviation: NME, nonmass enhancement.

spectral attenuated inversion recovery (SPAIR) fat suppression, TE = 82 ms, TR = 9,000 ms, *b*-values (number of diffusion directions) 6) 1,500 ,(6) 500 ,0 =), and 4,000 (15) seconds/mm^2, FOV = 160 × 320 mm^2, acquisition matrix = 48 × 96, reconstruction matrix = 128 × 128, voxel size = 2.5 × 2.5 × 5.0 mm^3, phase-encoding direction A/P, and no parallel imaging.

European dataset protocol

Unilateral sagittal DW-MRI was performed using Stejskal-Tanner spin-echo EPI including the following parameters: FatSat (n = 15) and SPAIR (n = 10) fat suppression, TE = 88 ms, TR = 10,600 ms (n = 15) and 11,800 ms (n = 10), *b*-values (number of diffusion directions) = 0, 200 (6), 600 (6), 1,200 (6), 1,800 (6), 2,400 (6), and 3,000 (6) seconds/mm^2, FOV = 180 × 180 mm^2, acquisition matrix = 90 × 90, reconstruction matrix = 90 × 90, voxel size = 2.0 × 2.0 × 2.5 mm^3, PE direction A/P, generalized autocalibrating partially parallel acquisition with acceleration factor of 2 and 24 reference lines.

Image processing and analysis

Noise correction (36) was performed to account for decreasing signal-to-noise ratio with increasing *b*-value. The observed signal (S_{obs}) is the mean signal across diffusion directions from one individual *b*-value image. Background voxels were selected by manually placing an ROI in an area in the air outside the breast on the highest *b*-value image, yielding the mean background intensity (S_{bkg}). The corrected signal intensity (S_{corr}) calculated from S_{obs} and S_{bkg} is given as:

$$S_{corr} = \sqrt{S_{obs}{}^2 - S_{bkg}{}^2} \quad (1)$$

$$S_{corr}(S_{corr} < 0) = 0$$

Furthermore, corrections for eddy current artifacts, motion (24), and geometric distortion (37) were applied for the European dataset.

Full-volume cancer and control ROIs were manually defined on DW-MRI images, guided by all available data in the exam protocol (including DCE-MRI and anatomic T2 images, **Fig. 1**), under

Downloaded from clincancerres.aacrjournals.org on October 19, 2021. © 2021 American Association for Cancer Research.

Published OnlineFirst November 4, 2020; DOI: 10.1158/1078-0432.CCR-20-2017

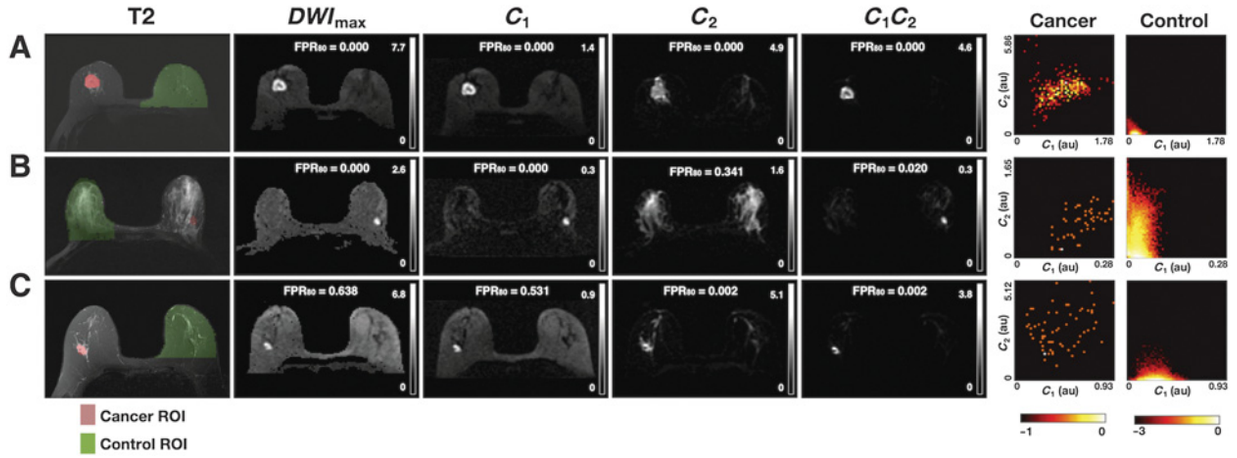

Figure 1.

Parameter maps for DWI_{max}, C_1, C_2, C_1C_2 with FPR_{80}, T2 images with cancer (red) and control (green) ROI overlay and probability density colormaps for cancer and control given C_1 and C_2 for three representative cases from the U.S. dataset. ROIs are here only displayed for one slice but are delineated for the full volume. FPR_{80} vary depending on the composition of healthy breast tissue in relation to the magnitude of C_1 and C_2 in cancer. **A,** Mixed tissue composition with cancer high on both dimensions. **B,** Abundant fibroglandular tissue and high C_1-magnitude of cancer. **C,** Abundant fatty tissue and high C_2-magnitude of cancer. DWI_{max} and C_1 performance is poorest in **C**, C_2 in **B** while C_1C_2 has perfect performance across cases. Colormaps are given on a logarithmic scale normalized to the maximum probability density value. *y*- and *x*-axis are defined by the maximum value for each case. Gray level windows for all images are scaled to the maximum and minimum signal intensity of each case and given in arbitrary unites. Au, arbitrary unit; C_i, signal contribution; DWI_{max}, image defined on maximum b-value; FPR_{80}, false-positive rate given sensitivity of 80%; ROI, region of interest.

supervision of and validation by two breast radiologists: R. Rakow-Penner (U.S. dataset) and A. Østlie (European dataset). Cancer ROIs were drawn for the lesions corresponding to pathology-proven cancer. Control ROIs were drawn for the entire contralateral breast (U.S. dataset) and in a cancer-free region in the ipsilateral breast at least 10 mm away from the cancer ROI (European dataset), with the aim to include all representative healthy breast tissue, excluding the axillary region, large cysts (>2.5 cm), and susceptibility artifacts. Cancer and control ROIs were used to determine discriminatory performance between cancer and healthy breast tissue, respectively.

For comparison with other DW-MRI methods, the nonnoise-corrected image defined on maximum *b*-value (DWI_{max}), conventional *ADC* (mono-exponential fitting of data), and apparent diffusion kurtosis (K_{app}) were estimated. DWI_{max} was acquired at $b = 4{,}000$ seconds/mm^2 for the U.S. dataset and $b = 3{,}000$ seconds/mm^2 for the European dataset. The exponential decay formulas described by Jensen and colleagues (38) and the corresponding *b*-value limits, <1,000 seconds/mm^2 and <2,000 seconds/mm^2, were used for computation of *ADC* and K_{app} maps, respectively. Note that *ADC* and K_{app} are calculated diffusion parameters where T2 and proton density dependence are eliminated (38).

To ensure that regions outside of the breast were not included in analysis, control ROIs were masked using intensity thresholding and three-dimensional connected components (U.S. dataset) or manually delineated within the breast boundary (European dataset) and reviewed by R. Rakow-Penner (U.S. dataset) and A. Østlie (European dataset) (**Figs. 1** and **4**). In addition, all undefined values (zero and infinite) on the image defined on $b = 0$ seconds/mm^2, *ADC*, and K_{app} were excluded.

Three-component modeling of diffusion signal

The corrected diffusion signal across all available *b*-values was fitted with a triexponential model, expressed as:

$$S_{corr}(b) = N\left[C_1 \cdot e^{-b \cdot ADC_1} + C_2 \cdot e^{-b \cdot ADC_2} + C_3 \cdot e^{-b \cdot ADC_3}\right] \quad (2)$$

where S_{corr} is the corrected diffusion signal in arbitrary units, b is the *b*-value in seconds/mm^2, and C_i denotes the voxelwise unitless signal contribution of each component. Note that $[C_1{+}C_2{+}C_3] \propto \rho{\cdot}\exp(-\mathrm{TE}/\mathrm{T2}_{eff})$, where ρ represents the proton density and $\mathrm{T2}_{eff}$ the effective T2 relaxation time in a given voxel. This model has been shown to represent the best fit across all voxels from both cancer and healthy breast tissue determined across patients, scanners, and sites (19), and yielded the fixed component *ADC* values used in this analysis: $ADC_1 = 0$ mm^2/second, $ADC_2 = 1.4 \times 10^{-3}$ mm^2/second, and $ADC_3 = 10.2 \times 10^{-3}$ mm^2/second. Fixing *ADCs* ensures linearization of the model and comparability of signal contributions across voxels and patients and avoids overfitting; the use of $ADC_1 = 0$ mm^2/second means this component behaves not as a distinct exponential as in other tissue (20, 21, 24, 39) but as a constant offset. Hence, we use the term "three-component" for the fitted model instead of "triexponential." All voxels were normalized to the 98th percentile of intensity within the $b = 0$ seconds/mm^2 image, indicated by the normalization factor (N). This was done to address different image intensity scaling while simultaneously preserving contribution of proton density and T2 to the DW-MRI signal.

Alternatively, the equation can be written by normalizing to the signal at $b = 0$ second/mm^2 per voxel (S_0), yielding signal fractions (F_i) rather than signal contributions (C_i). Thus, F_i is related directly to diffusion and more clearly separated from proton density and T2 properties, given as:

$$S_{corr}(b) = S_0\left[F_1 \cdot e^{-b \cdot ADC_1} + F_2 \cdot e^{-b \cdot ADC_2} + F_3 \cdot e^{-b \cdot ADC_3}\right] \quad (3)$$

where $F_1 + F_2 + F_3 = 1$ and $S(0) \propto \rho{\cdot}\exp(-\mathrm{TE}/\mathrm{T2}_{eff})$. This means that the signal contributions include voxelwise T2-weighting and proton density effects, while the signal fractions are only sensitive to diffusion component effects.

Downloaded from clincancerres.aacrjournals.org on October 19, 2021. © 2021 American Association for Cancer Research.

Published OnlineFirst November 4, 2020; DOI: 10.1158/1078-0432.CCR-20-2017

The following parametric maps were estimated from Equation 2: C_1C_2, C_1, and C_2. The parameters C_1 and C_2 were estimated directly from the model, while C_1C_2 is the corresponding product. Similarly, F_1F_2, F_1, and F_2 were estimated from Equation 3. The parametric maps C_3 and F_3 were not included because of the low cancer conspicuity of the third component (19). For completeness, the product of S_0 and signal fractions, $S_0F_1F_2$, S_0F_1, and S_0F_2, were estimated to investigate the relative importance of T2 and proton density effects.

Discriminating performance between cancer and healthy breast tissue

Clinical utility of the three-component derived parametric maps was assessed by comparing the voxelwise discriminatory performance between cancer (cancer ROIs) and healthy breast tissue (control ROIs) of C_1C_2, C_1, C_2, F_1F_2, F_1, F_2, $S_0F_1F_2$, S_0F_1, and S_0F_2 to DWI_{max}, ADC, and K_{app}. Because there were approximately 52 times more healthy breast tissue voxels than cancer voxels, performance in discriminating between cancer and healthy breast tissue was examined for all voxels by the expected false-positive rate given a sensitivity of 80% (FPR_{80}). In addition, the conventional performance measures ROC AUC, sensitivity, specificity, and accuracy were estimated. Sensitivity, specificity, and accuracy were calculated for the threshold value providing optimal accuracy, defined as the mean sensitivity and specificity, assuming equal prevalence of cancer and healthy breast tissue voxels. All three-component derived parametric maps, DWI_{max}, and K_{app} (29) were assumed to have higher intensity for cancer compared with healthy breast tissue, while the opposite was assumed for ADC (27, 28). Average signal of the cancer and control ROIs were calculated, and differences were compared using a Mann–Whitney U test with a threshold significance level of 0.05.

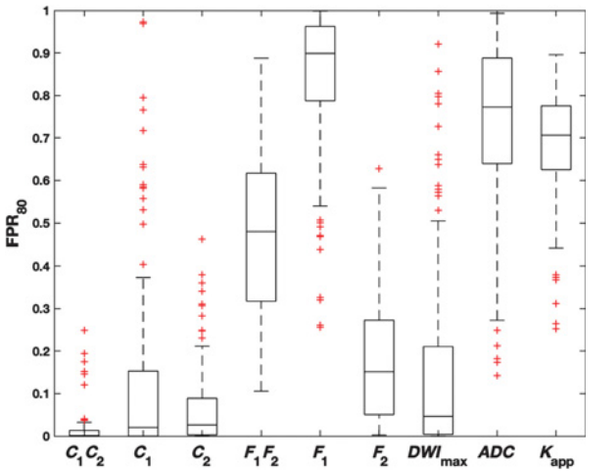

Figure 3.
The FPR_{80} is the false-positive rate given a sensitivity of 80% for discriminating cancer from healthy breast tissue for three-component model signal contributions (C_1C_2, C_1, C_2) and signal fractions (F_1F_2, F_1, F_2), DWI_{max}, ADC and K_{app}, given per patient across the U.S. and European dataset. Median values indicated by lines; boxes show interquartile range, block bars show data range and red crosses show outliers. The worst FPR_{80} for all maps is 0.9934, which would be 9,934 false-positive voxels of one breast (one control ROI) approximated to contain 10,000 voxels (~30 cL). ADC; conventional apparent diffusion coefficient; C_i, signal contribution; DWI_{max}, image defined on maximum b-value; F_i, signal fraction; K_{app}, apparent diffusion kurtosis.

Results

Sample

The total number of voxels from cancer and healthy breast tissue from both datasets was 37,659 and 1,946,186, respectively.

Optimized three-component model parameters for discrimination

Probability density colormaps for the three-component model given C_1 and C_2 including all voxels across patients and datasets are plotted for cancer (cancer ROIs, **Fig. 2A**) and healthy breast tissue (control ROIs, **Fig. 2B**). These maps display two distinct probability density distributions for cancer and healthy breast tissue. The product C_1C_2 discriminates cancer from healthy breast tissue voxels, where voxels low on one or two dimensions corresponds to healthy breast tissue voxels, while cancer probability increases with increased magnitude on C_1 and C_2.

The relationship between C_1 and C_2 demonstrates that voxels with high magnitude on both dimensions had the highest probability of cancer (**Fig. 1A**); representative cases are given in **Fig. 1**, and all cases are given in Supplementary Fig. S1–106. Discrimination performance varied depending on composition of healthy breast tissue in relation to the magnitude of C_1 and C_2 in cancer. FPR_{80} was higher (indicating more false-positive voxels) for C_1 and DWI_{max} in a case with abundant fat-suppressed fatty tissue and high C_2-magnitude of corresponding

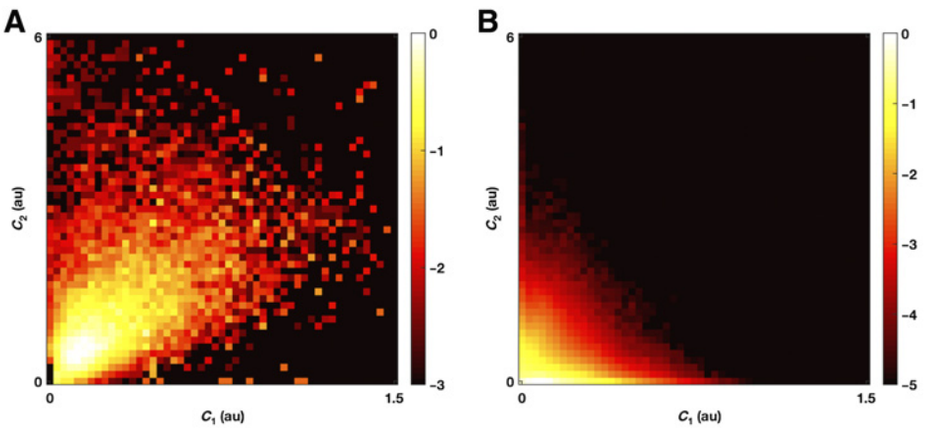

Figure 2.
Probability density colormaps for the three-component model given C_1 and C_2 including all voxels across patients and datasets are given for cancer (cancer ROIs; **A**) and healthy breast tissue (control ROIs; **B**). These maps display two distinct probability density distributions for cancer and healthy breast tissue. Cancer probability increases with increased magnitude on C_1 and C_2. Colormaps are given on a logarithmic scale normalized to the maximum probability density value. Au, arbitrary unit; C_i, signal contribution.

Downloaded from clincancerres.aacrjournals.org on October 19, 2021. © 2021 American Association for Cancer Research.

Published OnlineFirst November 4, 2020; DOI: 10.1158/1078-0432.CCR-20-2017

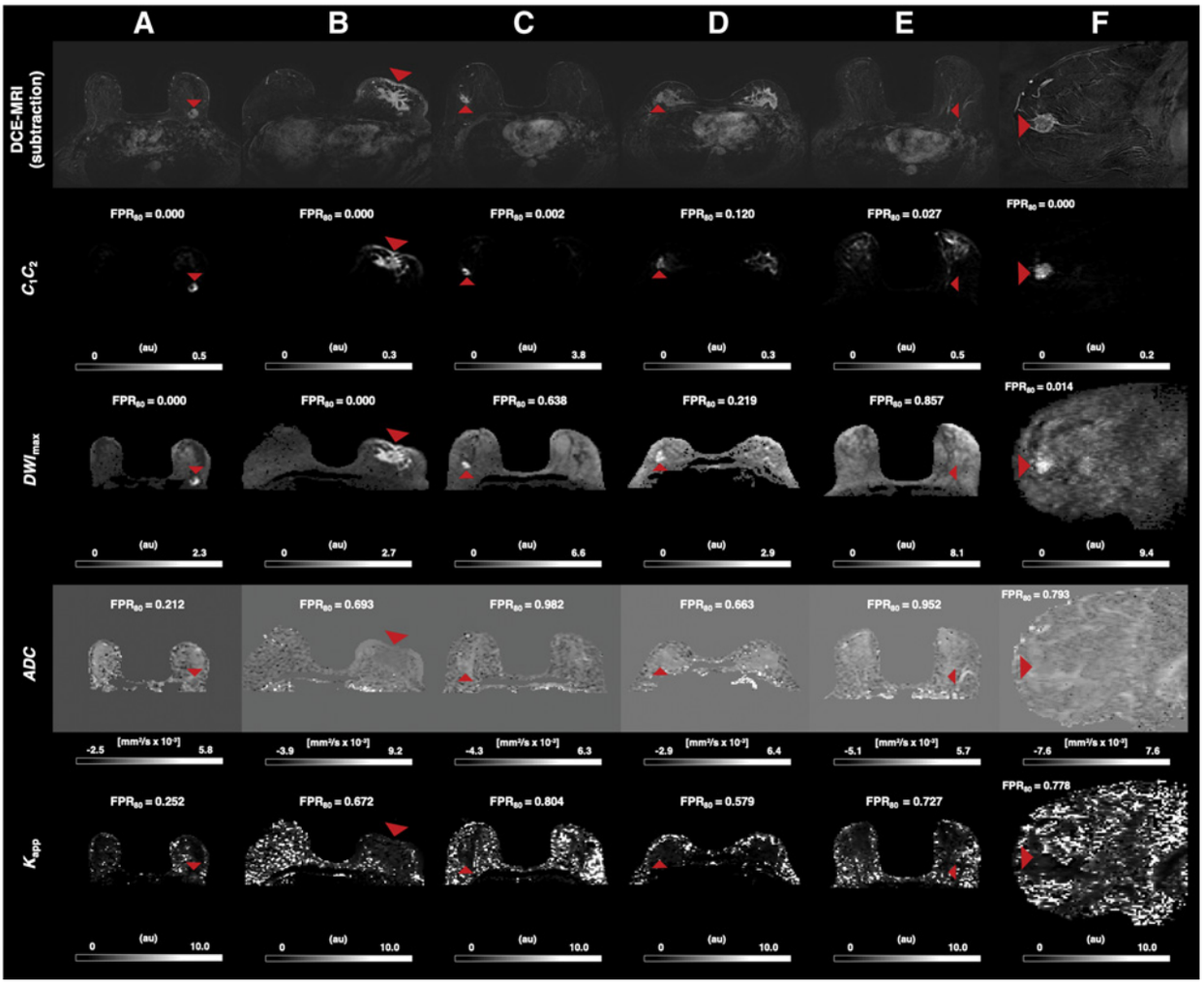

Figure 4.

C_1C_2, DWI_{max}, *ADC* and K_{app} with FPR_{80} for discrimination between cancer (red arrowhead) and healthy breast tissue (entire cancer-free contralateral breast for the U. S. dataset, cancer-free ipsilateral breast for the European dataset) for representative cases from the U.S. (**A–E**) and European (**F**) dataset. All cases demonstrate visual similarity between DCE-MRI and C_1C_2 maps with excellent performance compared with *ADC* and K_{app}. **A,** Excellent performance by C_1C_2 and DWI_{max}. **B,** Excellent performance by C_1C_2 and DWI_{max} displaying full extent of cancer involving skin. **C,** Excellent performance by C_1C_2 and poor performance by DWI_{max}, *ADC*, and K_{app} in a case with abundant fatty tissue. **D,** C_1C_2 improves poor DCE-MRI specificity in a case with marked background parenchymal enhancement, but partial volume artifact from the interface of fibroglandular and fatty tissue in the contralateral breast results in a low discriminatory performance. **E,** A case with NME DCIS where all diffusion maps fail; C_1C_2 has reduced signal intensity from cancer relative to the high-signal intensity from ipsilateral subareolar ducts. **F,** Sagittal image plane illustrating same trends in the European dataset. The worst FPR_{80} for all maps is 0.9934, which would be 9,934 false-positive voxels of one breast (one control ROI) approximated to contain 10,000 voxels (~30 cL). Gray level windows for all images are scaled to the maximum and minimum signal intensity of each case. *ADC*, conventional apparent diffusion coefficient; Au, arbitrary unit; C_i, signal contribution; DCE-MRI, dynamic contrast-enhanced MRI; DCIS; ductal carcinoma *in situ*; DWI_{max}, image defined on maximum *b*-value; FPR_{80}, false-positive rate given sensitivity of 80%; K_{app}, apparent diffusion kurtosis; NME; nonmass enhancement.

cancer (**Fig. 1C**), compared with abundant fibroglandular tissue and high C_1-magnitude of corresponding cancer (**Fig. 1B**). The opposite was seen for C_2, while C_1C_2 suppressed both fibroglandular and fatty tissue. This shows that the C_1C_2 parameter derived from the three-component model provided the optimal discrimination performance between cancer and healthy breast tissue.

All signal contributions (C_1C_2, C_1, C_2) performed better than signal fractions (F_1F_2, F_1, and F_2), given in **Fig. 3**. Signal fractions where S_0 was included ($S_0F_1F_2$, S_0F_1 and S_0F_2) performed nearly equal to corresponding signal contributions (C_1C_2, C_1, C_2; see Supplementary Tables S1 and S2).

Discriminatory performance of C_1C_2 compared with other DW-MRI methods

Mean FPR_{80} for both datasets was 0.016 (95% CI, 0.008–0.024) for C_1C_2, 0.136 (95% CI, 0.092–0.180) for C_1, 0.068 (95% CI, 0.049–0.087) for C_2, 0.462 (95% CI, 0.425–0.499) for F_1F_2, 0.832 (95% CI, 0.797–0.868) for F_1, 0.176 (95% CI, 0.150–0.203) for F_2, 0.159 (95% CI, 0.114–0.204) for DWI_{max}, 0.731 (95% CI, 0.692–0.770) for *ADC*, and 0.684 (95% CI, 0.660–0.709) for K_{app} (**Fig. 3**). C_1C_2 achieved the lowest FPR_{80} with a mean ROC AUC of 0.984 (95% CI, 0.977–0.991) when compared with other DW-MRI methods. Discriminatory performance was similar across datasets; see Supplementary Tables S1 and

Downloaded from clincancerres.aacrjournals.org on October 19, 2021. © 2021 American Association for Cancer Research.

Published OnlineFirst November 4, 2020; DOI: 10.1158/1078-0432.CCR-20-2017

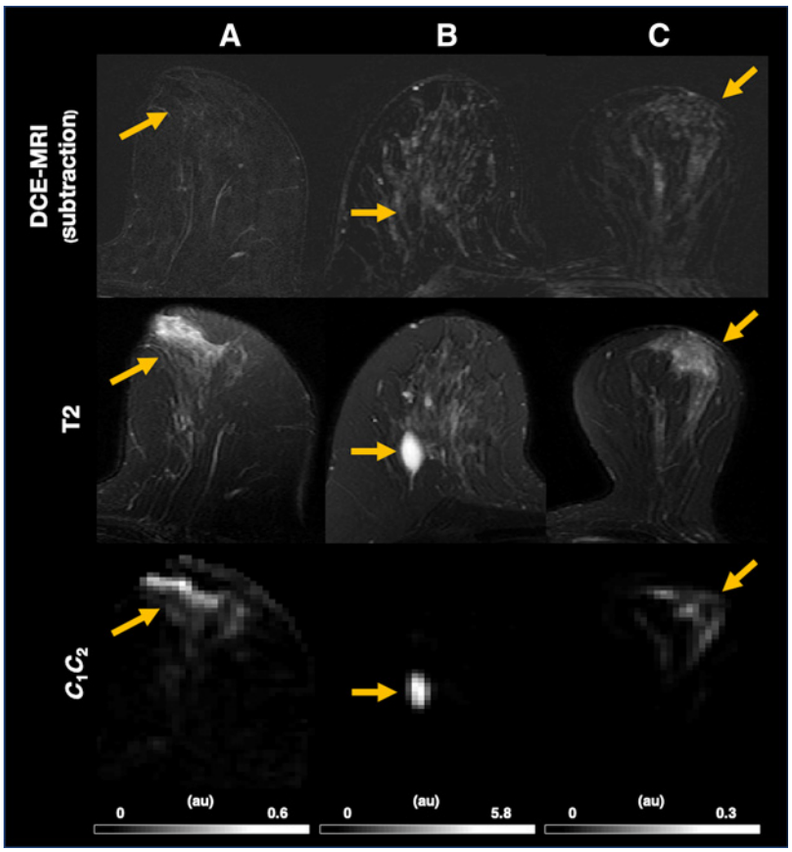

Figure 5.
DCE-MRI and T2 images with corresponding C_1C_2 images illustrating false positives on C_1C_2 (yellow arrow). **A** and **B,** Show that false-positive lesions on C_1C_2 can be defined as nonsuspicious with the assistance of T2 images by a hyperintense signal on the T2 image correlated with clearly benign morphology. **A,** High signal involving subareolar ducts on T2 image and C_1C_2, not visible on DCE-MRI. **B,** Cyst visible on T2 image and C_1C_2, not visible on DCE-MRI. **C,** Demonstration of limitation of C_1C_2 where background parenchymal enhancement visible on DCE-MRI and T2 image creates a partial volume artifact corresponding to the interface between fatty and fibroglandular tissue on C_1C_2. Au, arbitrary unit; C_i, signal contribution; DCE-MRI, dynamic contrast-enhanced MRI.

S2 for all conventional performance measures and FPR_{80} given for the two datasets separately. Average signal of the cancer and control ROIs are shown in Supplementary Table S3. All cancer and control ROIs were significantly different ($P < 1 \times 10^{-9}$).

C_1C_2 had excellent performance compared with ADC and K_{app} in a wide range of representative cases (**Fig. 4**). DWI_{max} performs well in several cases (**Fig. 4A** and **B**) but underperforms compared with C_1C_2, overall (**Fig. 3**) and particularly in a case with abundant fatty tissue (**Fig. 4C**). In addition, C_1C_2 visually improves poor DCE-MRI specificity in a case with marked background parenchymal enhancement (**Fig. 4D**). However, C_1C_2 underperforms in cases with sparse signal from cancer, such as case of nonmass enhancement (NME) ductal carcinoma in situ (DCIS; **Fig. 4E**). In this case, all DW-MRI–derived maps failed to identify cancer compared with healthy breast tissue. Furthermore, there was high diffusion signal from some healthy breast tissue components such as proteinaceous cysts (**Fig. 5B**), subareolar ducts (**Fig. 5A**), and partial volume artifact from the interface of fibroglandular and fatty tissue (**Fig. 4D** and **Fig. 5C**). High diffusion signal from proteinaceous cysts and subareolar ducts may be defined as nonsuspicious with the assistance of T2 images (**Fig. 5A** and **B**).

Discussion

Our study shows that cancer can be noninvasively discriminated from healthy breast tissue using the derived parameter C_1C_2 based on a three-component DW-MRI model, with results comparable with cancer detection using DCE-MRI (refs. 2–6; FPR_{80} mean, 0.016; 95% CI, 0.008–0.024 and ROC AUC mean, 0.984; 95% CI, 0.977–0.991). This means that C_1C_2 achieved very low false-positive rates while detecting 80% or more of the defined cancer voxels. The discriminatory power of C_1C_2 was superior to that of independent signal contributions and signal fractions, conventional DW-MRI-estimates (ADC) and other methods, including diffusion kurtosis imaging (K_{app}) and DWI_{max}. The three-component model was performed across two different sites, scanners, and acquisition protocols, suggesting potential for clinical applications. The development of this advanced DW-MRI method allows for improved conspicuity of cancer relative to background breast tissue. This lays the foundation for a quantitative framework specific to pathology which may serve as an alternative to DCE-MRI.

The high discriminatory performance is due to the characteristics of the novel C_1C_2 parameter. In addition to malignancy, individual signal contributions from the three-component model were sensitive to the two primary components of healthy breast tissue: fatty (C_1) and fibroglandular (C_2) tissue. As the lipid component of fatty tissue signal is suppressed by application of fat suppression in this study (SPAIR and FatSat), we hypothesize that signal on C_1 comes from the restricted water component within adipocytes in fatty tissue (18, 19). Furthermore, neither component was sensitive to tissue with very fast diffusion properties, such as vessels, necrosis, or edema. By combining the signal contributions of the two slowest components C_1 and C_2, the majority of signal from fatty and fibroglandular tissue was suppressed so that the output image was predominantly sensitive to cancer compared with healthy breast tissue. This is particularly useful because of the varying degree of

Downloaded from clincancerres.aacrjournals.org on October 19, 2021. © 2021 American Association for Cancer Research.

Published OnlineFirst November 4, 2020; DOI: 10.1158/1078-0432.CCR-20-2017

admixture of fatty and fibroglandular tissue in the breast. In fact, histologic evaluation of healthy breast tissue specimen demonstrated on average 29.7% fatty tissue component in dense breasts and 80.6% in nondense breasts (15). Thus, C_1C_2 may account for women with varying degree of admixed fatty tissue which is known to be an issue on conventional DW-MRI (16). While optimized for cancer discrimination, the detailed relationship between the three-component model and breast microstructure remains to be studied, as it has been for the two-component model (34, 40).

Another important aspect attributing to the high discriminatory performance is the retainment of T2 and proton density contribution to the DW-MRI signal. On conventional DW-MRI, T2 effects on DW-MRI signal is considered an inconvenience and is therefore eliminated (41). In this study, we present signal contributions that include contribution from voxelwise proton density and T2, while the signal fractions are defined to only be sensitive to diffusion effects. Thus, the importance of T2 and proton density is clearly demonstrated by the signal contributions C_1C_2, C_1, and C_2 performing far better than their signal fraction counterparts F_1F_2, F_1, and F_2. We further see these effects by signal fractions performing nearly equal to corresponding signal contributions once the signal at $b = 0$ second/mm^2, S_0, was included, which demonstrates that $C_i \approx S_0F_i$. This has also been shown in separating benign and malignant breast lesions, where S_0 (which has no diffusion weighting), yielded a relatively high AUC of 0.85 (12).

We hypothesize that contributing factors to the poor performance of *ADC* and K_{app} include the restricted water component within adipocytes in fatty tissue not accounted for by fat suppression techniques and elimination of proton density and T2 effects that add to cancer discrimination. The FPR_{80} discriminatory performance of *ADC* and K_{app} varied greatly across subjects; at best, performing around 0.2 in selected cases (**Fig. 4A**), but overall do no better than chance. Previous studies have demonstrated significant differences between cancer and healthy breast tissue by *ADC* (27, 28) and K_{app} (29). However, these studies have been performed by signal averaged across ROIs and not voxelwise, which does not reflect the heterogeneity of healthy breast tissue including admixture of fatty and fibroglandular tissue. Conversely, DWI_{max} shares the same basic properties as C_1C_2 (diffusion-, T2-, and proton density–weighting) and performs noticeably better than *ADC* and K_{app} and have several cases with perfect performance (**Fig. 1A** and **B** and **Fig. 4A** and **B**). However, DWI_{max} is also prone to influence from restricted water from fatty tissue and performs worse than C_1C_2 on average. C_1C_2 better accounts for all healthy breast tissue including the restricted water component from fatty tissue, conferring a major advantage over DWI_{max} and the other DWI estimates (**Fig. 4C**), as fibroglandular tissue is admixed with fatty tissue, and approximately 50% of women have almost entirely fatty breast tissue or scattered fibroglandular tissue (42).

For C_1C_2 to be a noninvasive alternative to DCE-MRI for breast cancer detection, it must have comparable or improved sensitivity and specificity. DW-MRI is known to improve detection specificity (8, 43), which is beneficial as lesion-level DCE-MRI specificity have been reported to range from 72% to 97% (2–6). In our study, performance was assessed per voxel, and the patient cohort was heterogenous, consisting of a large range of tumor volumes (mean, 10.6 cm^3; range, 0.2–105.9 cm^3), not reflecting the typical patient pool in the screening or surveillance setting which typically have smaller lesions. However, the high performance of discriminating cancer from all other breast tissue in comparison with other DW-MRI–based methods is highly promising and suggests clinical utility comparable with DCE-MRI. C_1C_2 may be particularly useful when DCE-MRI demonstrates false-positive (**Fig. 4D**; ref. 44) and false-negative (45) interpretations in patients with moderate and marked background parenchymal enhancement. Furthermore, false-positive findings on C_1C_2 can be defined as nonsuspicious by a hyperintense signal on the T2 image correlated with clearly benign morphology (**Fig. 5A** and **B**). While proteinaceous cysts (**Fig. 5B**) are well-known false positives on DW-MRI (46), subareolar ducts (**Fig. 5A**) are not commonly reported and may be due to T2 influence on C_1C_2. This indicates that C_1C_2 may assist in a noncontrast workflow with anatomic T1 and/or T2 sequences which can remove the need to administer gadolinium contrast and any accumulation of gadolinium in the brain (7).

The three-component model lays the foundation for a computationally efficient and standardized framework for breast cancer detection generalizable across sites, scanners, and acquisition protocols. By using globally determined, fixed component *ADC*s, the three-component model allows for rapid fitting of diffusion signal suitable for application as a turn-key processing stream on both GE and Siemens platforms. These factors are vital for implementation in standard-of-care breast MRI. Furthermore, the three-component model is performed on data acquired on extended imaging protocols (b-values up to 3,000–4,000 seconds/mm^2) and requires at least three separate nonzero b-values. Inclusion of higher b-values improves discrimination by allowing better estimates of very slow diffusion characteristics of intracellular fluid within hypercellular tumors (9–12, 20–26). However, high b-value acquisition also results in an increased scan time, where the protocol used for the European dataset in this study for (including seven b-values up to 3,000 seconds/mm^2) had a scan time of approximately 8 minutes compared with a standard DW-MRI protocol (including two b-values) which are typically performed in 1–3 minutes. We argue that the substantially increased discriminatory performance of the derived C_1C_2 parameter compared with conventional DW-MRI justifies the increase in scan time, which is also the same scan time as conventional DCE-MRI. This does, however, illustrate the need for optimized b-value protocols for improved scan time efficiency, which is an area of interest for future development.

Several diffusion methods aim to isolate the signal from the slowly diffusing water component from cancer tissue by utilizing broad b-value ranges (9–12, 20–26). Diffusion kurtosis imaging is based on a simple mathematical representation of diffusion data where the derived parameter K_{app} has proven potential utility in the breast (9–11, 29). More advanced, multicomponent partial volume models with fixed *ADC*s have been developed to further probe the microstructure in the brain and prostate: RSI (refs. 24–26; on which the three-component model is based), the vascular, extracellular, and restricted diffusion for cytometry in tumors (VERDICT) model (21), and the hybrid multidimensional MRI model (22). A key difference between RSI/three-component model and the hybrid multidimensional MRI model is that the hybrid model does not use predetermined, fixed component *ADC*s, making comparison of corresponding signal contributions across patients and voxels difficult. Nevertheless, the hybrid model does incorporate multiecho information not available in our study. Moreover, the T2 and proton density effects seen in RSI/three-component model are removed from the two other models, potentially reducing cancer conspicuity. Although the other multicomponent partial

Downloaded from clincancerres.aacrjournals.org on October 19, 2021. © 2021 American Association for Cancer Research.

Published OnlineFirst November 4, 2020; DOI: 10.1158/1078-0432.CCR-20-2017

volume models have shown promising results as cancer biomarkers in the prostate, for example, these results may be limited in breast, where fatty tissue is an important component of healthy breast tissue.

The three-component model may share biophysical similarities with the two-component intravoxel incoherent motion (IVIM) model (47). The two fastest component *ADCs* from the three-component model, $ADC_2 = 1.4 \times 10^{-3}$ mm^2/second and $ADC_3 = 10.2 \times 10^{-3}$ mm^2/second, are an order of magnitude apart and in the range of diffusion coefficients typically fitted for an IVIM model in breast tissue ("pure tissue diffusion coefficient" and "pseudodiffusion coefficient"; refs. 48, 49). Therefore, we interpret that ADC_2 and the "pure tissue diffusion coefficient" from IVIM represent hindered diffusion of fibroglandular tissue, while ADC_3 and the "pseudodiffusion coefficient" from IVIM represent the very fast diffusion properties from pseudodiffusion/perfusion. This means that the optimized three-component model by Rodríguez-Soto and colleagues (19) is similar to an IVIM model with an additional offset C_1 with $ADC_1 = 0$ mm^2/second, which manifests in the high *b*-value range and accounts for the restricted water component in fatty tissue. The IVIM model focuses on perfusion properties fit to mid *b*-value data (typically up to 800–1,000 seconds/mm^2) and are therefore not sensitized to these very restricted diffusion properties. Moreover, as previously discussed, signal contributions include voxelwise T2-weighting and proton density effects which is very important for discriminatory performance, while the signal fractions were only sensitive to diffusion component effects, and as such are more directly comparable with the signal fractions in an IVIM model.

There were some limitations to our study. First, the three-component methodology did not correct for partial volume artifacts which occurred at the interface between fatty and fibroglandular tissue on C_1C_2 (**Fig. 4D** and **Fig. 5C**). Such artifacts have the potential to be corrected, which was not investigated in this study but is an area of interest for future improvement. Another limitation concerned the definition of control ROIs; although we ensured that all control ROIs were verified as cancer-free, based on MRI review by an expert breast radiologist (both datasets) and exclusion of cases with pathology-proven contralateral cancer in the U.S. dataset, we cannot know whether occult cancer may have been included in the control ROIs. The unilateral European dataset may have been particularly prone to this, as the control ROIs were defined in the same breast as the cancer (this also made the size of control ROIs dependent on the extent of cancer and thus variable from case to case in that dataset). Finally, detection performance is commonly evaluated at the lesion level. This study used a voxelwise false-positive rate, FPR_{80}, as its performance measure, which does not give an absolute measure comparable with other literature. However, we argue that such a measure is useful from a radiologist's perspective, because it mimics a breast cancer examination where all voxels in the entire image are used.

In conclusion, our study is the first to demonstrate that the derived parameter C_1C_2, which is the product of the two slowest components of a three-component DW-MRI model, yields a clinically useful, non-invasive method for discrimination between cancer and healthy breast tissue. The model eliminates the need for predefined lesions that conventional quantitative DW-MRI metrics use and accounts for all healthy breast tissue, including the restricted water component from fatty tissue. Together with anatomic images, C_1C_2 has the potential to assist in a combined, noncontrast workflow which could serve as an alternative to DCE-MRI. The highly promising diagnostic properties were generalized across sites, scanners, and acquisition protocols, which is important for feasibility of large-scale studies for validation in routine breast cancer detection and follow-up in comparison with DCE-MRI.

Authors' Disclosures

M.M.S. Andreassen reports grants from Fulbright Scholarship Program during the conduct of the study. A.E. Rodríguez-Soto reports grants from GE Healthcare during the conduct of the study. I. Vidić reports personal fees from Cortechs labs, Inc. outside the submitted work. T.M. Seibert reports grants from NIH during the conduct of the study; personal fees from Varian Medical Systems, Multimodal Imaging Services Corporation, and WebMD outside the submitted work. M.E. Hahn reports grants from General Electric during the conduct of the study; personal fees from HealthLytix and Illumina outside the submitted work. T.F. Bathen reports grants from Liaison Committee between the Central Norway Regional Health Authority (RHA) and the Norwegian University of Science and Technology (NTNU) during the conduct of the study. H. Ojeda-Fournier reports personal fees from IBM Watson and ViewPoint Medical outside the submitted work R. Rakow-Penner reports grants from California Breast Cancer Research Program and General Electric during the conduct of the study; personal fees from Human Longevity Inc outside the submitted work. A.M. Dale reports grants from NIH and General Electric Healthcare during the conduct of the study; grants from NIH outside the submitted work; a patent for US20120280686 licensed to General Electric and a patent for US9568580B2 licensed to General Electric; and A.M. Dale is a Founder of and holds equity in CorTechs Labs, Inc. and is a member of the scientific advisory board of Human Longevity, Inc. (The terms of these arrangements have been reviewed and approved by UCSD, in accordance with its conflict of interest policies). No disclosures were reported by the other authors.

Authors' Contributions

M.M.S. Andreassen: Formal analysis, investigation, writing-original draft, writing-review and editing. **A.E. Rodríguez-Soto:** Data curation, software, formal analysis, supervision, validation, investigation, methodology, writing-original draft, project administration, writing-review and editing. **C.C. Conlin:** Methodology, writing-original draft, writing-review and editing. **I. Vidić:** Methodology, writing-review and editing. **T.M. Seibert:** Supervision, methodology, writing-original draft, writing-review and editing. **A.M. Wallace:** Investigation. **S. Zare:** Validation, investigation. **J. Kuperman:** Data curation, methodology. **B. Abudu:** Data curation, investigation. **G.S. Ahn:** Data curation, investigation. **M. Hahn:** Supervision. **N.P. Jerome:** Supervision, writing-review and editing. **A. Østlie:** Data curation. **T.F. Bathen:** Supervision. **H. Ojeda-Fournier:** Validation, investigation. **P.E. Goa:** Supervision, methodology, writing-review and editing. **R. Rakow-Penner:** Conceptualization, resources, data curation, supervision, funding acquisition, validation, investigation, visualization, methodology, project administration, writing-review and editing. **A.M. Dale:** Conceptualization, resources, software, formal analysis, supervision, funding acquisition, validation, investigation, methodology, project administration, writing-review and editing.

Acknowledgments

We would like to acknowledge the financial support from the California Breast Cancer Research Program Early Career Award (to R. Rakow-Penner), California Breast Cancer Screening Program grant No. 25IB-0056 (To R. Rakow-Penner), GE Healthcare (to R. Rakow-Penner and A.M. Dale), NIH/NIBIB grant No. K08EB026503 (to T.M. Seibert), and the Fulbright Scholarship Program (to M.M.S. Andreassen).

The costs of publication of this article were defrayed in part by the payment of page charges. This article must therefore be hereby marked *advertisement* in accordance with 18 U.S.C. Section 1734 solely to indicate this fact.

Received May 28, 2020; revised August 29, 2020; accepted October 29, 2020; published first November 4, 2020.

Downloaded from clincancerres.aacrjournals.org on October 19, 2021. © 2021 American Association for Cancer Research.

Published OnlineFirst November 4, 2020; DOI: 10.1158/1078-0432.CCR-20-2017

References

1. Lehman CD, Blume JD, Weatherall P, Thickman D, Hylton N, Warner E, et al. Screening women at high risk for breast cancer with mammography and magnetic resonance imaging. Cancer 2005;103:1898–905.
2. Kuhl CK, Schrading S, Leutner CC, Morakkabati-Spitz N, Wardelmann E, Fimmers R, et al. Mammography, breast ultrasound, and magnetic resonance imaging for surveillance of women at high familial risk for breast cancer. J Clin Oncol 2005;23:8469–76.
3. Kriege M, Brekelmans CTM, Boetes C, Besnard PE, Zonderland HM, Obdeijn IM, et al. Efficacy of MRI and mammography for breast-cancer screening in women with a familial or genetic predisposition. N Engl J Med 2004;351: 427–37.
4. Leach MO, Boggis CR, Dixon AK, Easton DF, Eeles RA, Evans DGR, et al. Screening with magnetic resonance imaging and mammography of a UK population at high familial risk of breast cancer: a prospective multicentre cohort study (MARIBS). Lancet 2005;365:1769–78.
5. Saadatmand S, Geuzinge HA, Rutgers EJT, Mann RM, de Roy van Zuidewijn DBW, Zonderland HM, et al. MRI versus mammography for breast cancer screening in women with familial risk (FaMRIsc): a multicentre, randomised, controlled trial. Lancet Oncol 2019;20:1136–47.
6. Peters NHGM, Borel Rinkes IHM, Zuithoff NPA, Mali WPTM, Moons KGM, Peeters PHM. Meta-analysis of MR imaging in the diagnosis of breast lesions. Radiology 2008;246:116–24.
7. Gulani V, Calamante F, Shellock FG, Kanal E, Reeder SB. Gadolinium deposition in the brain: summary of evidence and recommendations. Lancet Neurol 2017; 16:564–70.
8. Chen X, Li W-L, Zhang Yi-Li, Wu Q, Guo Y-M, Bai Z-L. Meta-analysis of quantitative diffusion-weighted MR imaging in the differential diagnosis of breast lesions. BMC Cancer 2010;10:693.
9. Wu D, Li G, Zhang J, Chang S, Hu J, Dai Y. Characterization of breast tumors using diffusion kurtosis imaging (DKI). PLoS One 2014;9:e113240.
10. Christou A, Ghiatas A, Priovolos D, Veliou K, Bougias H. Accuracy of diffusion kurtosis imaging in characterization of breast lesions. Br J Radiol 2017;90: 20160873.
11. Nogueira L, Brandão S, Matos E, Nunes RG, Loureiro J, Ramos I, et al. Application of the diffusion kurtosis model for the study of breast lesions. Eur Radiol 2014;24:1197–203.
12. Vidić I, Egnell L, Jerome NP, White NS, Karunamuni R, Rakow-Penner R, et al. Modeling the diffusion-weighted imaging signal for breast lesions in the b = 200 to 3000 s/mm(2) range: quality of fit and classification accuracy for different representations. Magn Reson Med 2020;84:1011–23.
13. Luo J, Hippe DS, Rahbar H, Parsian S, Rendi MH, Partridge SC. Diffusion tensor imaging for characterizing tumor microstructure and improving diagnostic performance on breast MRI: a prospective observational study. Breast Cancer Res 2019;21:102.
14. Iima M, Kataoka M, Kanao S, Onishi N, Kawai M, Ohashi A, et al. Intravoxel Incoherent motion and quantitative non-gaussian diffusion MR imaging: evaluation of the diagnostic and prognostic value of several markers of malignant and benign breast lesions. Radiology 2018;287:432–41.
15. Ghosh K, Brandt KR, Reynolds C, Scott CG, Pankratz VS, Riehle DL, et al. Tissue composition of mammographically dense and non-dense breast tissue. Breast Cancer Res Treat 2012;131:267–75.
16. Partridge SC, Singer L, Sun R, Wilmes LJ, Klifa CS, Lehman CD, et al. Diffusion-weighted MRI: influence of intravoxel fat signal and breast density on breast tumor conspicuity and apparent diffusion coefficient measurements. Magn Reson Imaging 2011;29:1215–21.
17. Delfaut EM, Beltran J, Johnson G, Rousseau J, Marchandise X, Cotten A. Fat suppression in MR imaging: techniques and pitfalls. Radiographics 1999;19: 373–82.
18. Baron P, Dorrius MD, Kappert P, Oudkerk M, Sijens PE. Diffusion-weighted imaging of normal fibroglandular breast tissue: influence of microperfusion and fat suppression technique on the apparent diffusion coefficient. NMR Biomed 2010;23:399–405.
19. Rodriguez-Soto AE, Andreassen MMS, Conlin CC, Park HH, Ahn GS, Bartsch H, et al. Characterization of the diffusion signal of breast tissues using multi-exponential models. https://doi.org/10.1101/2020.04.27.20082271.
20. Karunamuni RA, Kuperman J, Seibert TM, Schenker N, Rakow-Penner R, Sundar VS, et al. Relationship between kurtosis and bi-exponential characterization of high b-value diffusion-weighted imaging: application to prostate cancer. Acta Radiol 2018;59:1523–29.
21. Panagiotaki E, Chan RW, Dikaios N, Ahmed HU, O'Callaghan J, Freeman A, et al. Microstructural characterization of normal and malignant human prostate tissue with vascular, extracellular, and restricted diffusion for cytometry in tumours magnetic resonance imaging. Invest Radiol 2015;50: 218–7.
22. Chatterjee A, Bourne RM, Wang S, Devaraj A, Gallan AJ, Antic T, et al. Diagnosis of prostate cancer with noninvasive estimation of prostate tissue composition by using hybrid multidimensional MR imaging: a feasibility study. Radiology 2018; 287:864–73.
23. Rakow-Penner RA, White NS, Parsons JK, Choi HW, Liss MA, Kuperman JM, et al. Novel technique for characterizing prostate cancer utilizing MRI restriction spectrum imaging: proof of principle and initial clinical experience with extraprostatic extension. Prostate Cancer Prostatic Dis 2015;18: 81–5.
24. White NS, McDonald CR, Farid N, Kuperman J, Karow D, Schenker-Ahmed NM, et al. Diffusion-weighted imaging in cancer: physical foundations and applications of restriction spectrum imaging. Cancer Res 2014;74: 4638–52.
25. White NS, Leergaard TB, D'Arceuil H, Bjaalie JG, Dale AM. Probing tissue microstructure with restriction spectrum imaging: Histological and theoretical validation. Hum Brain Mapp 2013;34:327–46.
26. White NS, McDonald CR, Farid N, Kuperman JM, Kesari S, Dale AM. Improved conspicuity and delineation of high-grade primary and metastatic brain tumors using "restriction spectrum imaging": quantitative comparison with high B-value DWI and ADC. AJNR Am J Neuroradiol 2013;34:958–64.
27. Woodhams R, Matsunaga K, Iwabuchi K, Kan S, Hata H, Kuranami M, et al. Diffusion-weighted imaging of malignant breast tumors: the usefulness of apparent diffusion coefficient (ADC) value and ADC map for the detection of malignant breast tumors and evaluation of cancer extension. J Comput Assist Tomogr 2005;29:644–9.
28. Jin Ya-N, Zhang Y, Cheng J-L, Zheng D-D, Hu Y. Monoexponential, biexponential, and stretched-exponential models using diffusion-weighted imaging: a quantitative differentiation of breast lesions at 3.0T. J Magn Reson Imaging 2019; 50:1461–67.
29. Zhou WP, Zan XY, Hu XY, Liu X, Sudarshan SKP, Yang S-D, et al. Characterization of breast lesions using diffusion kurtosis model-based imaging: an initial experience. J Xray Sci Technol 2020;28:157–69.
30. Vidić I, Egnell L, Jerome NP, Teruel JR, Sjøbakk TE, Østlie A, et al. Support vector machine for breast cancer classification using diffusion-weighted MRI histogram features: preliminary study. J Magn Reson Imaging 2018; 47:1205–16.
31. Teruel JR, Goa PE, Sjøbakk TE, Østlie A, Fjøsne HE, Bathen TF. Diffusion weighted imaging for the differentiation of breast tumors: from apparent diffusion coefficient to high order diffusion tensor imaging. J Magn Reson Imaging 2016;43:1111–21.
32. Vidić I, Jerome NP, Bathen TF, Goa PE, While PT. Accuracy of breast cancer lesion classification using intravoxel incoherent motion diffusion-weighted imaging is improved by the inclusion of global or local prior knowledge with bayesian methods. J Magn Reson Imaging 2019;50:1478–88.
33. Teruel JR, Goa PE, Sjøbakk TE, Østlie A, Fjøsne HE, Bathen TF. A simplified approach to measure the effect of the microvasculature in diffusion-weighted MR imaging applied to breast tumors: preliminary results. Radiology 2016;281: 373–81.
34. Egnell L, Vidić I, Jerome NP, Bofin AM, Bathen TF, Goa PE. Stromal collagen content in breast tumors correlates with in vivo diffusion-weighted imaging: a comparison of multi b-value DWI with histologic specimen from benign and malignant breast lesions. J Magn Reson Imaging 2020;51: 1868–78.
35. Teruel JR, Fjøsne HE, Østlie A, Holland D, Dale AM, Bathen TF, et al. Inhomogeneous static magnetic field-induced distortion correction applied to diffusion weighted MRI of the breast at 3T. Magn Reson Med 2015;74:1138–44.
36. Gudbjartsson H, Patz S. The Rician distribution of noisy MRI data. Magn Reson Med 1995;34:910–4.
37. Holland D, Kuperman JM, Dale AM. Efficient correction of inhomogeneous static magnetic field-induced distortion in Echo Planar Imaging. Neuroimage 2010;50:175–83.
38. Jensen JH, Helpern JA, Ramani A, Lu H, Kaczynski K. Diffusional kurtosis imaging: the quantification of non-gaussian water diffusion by means of magnetic resonance imaging. Magn Reson Med 2005;53:1432–40.

Downloaded from clincancerres.aacrjournals.org on October 19, 2021. © 2021 American Association for Cancer Research.

Published OnlineFirst November 4, 2020; DOI: 10.1158/1078-0432.CCR-20-2017

39. Panagiotaki E, Walker-Samuel S, Siow B, Johnson SP, Rajkumar V, Pedley RB, et al. Noninvasive quantification of solid tumor microstructure using VERDICT MRI. Cancer Res 2014;74:1902–12.
40. Tamura T, Usui S, Murakami S, Arihiro K, Fujimoto T, Yamada T, et al. Comparisons of multi b-value DWI signal analysis with pathological specimen of breast cancer. Magn Reson Med 2012;68:890–7.
41. Provenzale JM, Engelter ST, Petrella JR, Smith JS, MacFall JR. Use of MR exponential diffusion-weighted images to eradicate T2 "shine-through" effect. AJR Am J Roentgenol 1999;172:537–9.
42. American College of Radiology: Breast density: breast cancer screening. Available from: https://www.acr.org/-/media/ACR/Files/Breast-Imaging-Resources/Breast-Density-bro_ACR_SBI.pdf.
43. Tsushima Y, Takahashi-Taketomi A, Endo K. Magnetic resonance (MR) differential diagnosis of breast tumors using apparent diffusion coefficient (ADC) on 1.5-T. J Magn Reson Imaging 2009;30:249–55.
44. Giess CS, Raza S, Birdwell RL. Patterns of nonmasslike enhancement at screening breast MR imaging of high-risk premenopausal women. Radiographics 2013;33:1343–60.
45. Shimauchi A, Jansen SA, Abe H, Jaskowiak N, Schmidt RA, Newstead GM. Breast cancers not detected at MRI: review of false-negative lesions. AJR Am J Roentgenol 2010;194:1674–9.
46. Telegrafo M, Rella L, Stabile Ianora AA, Angelelli G, Moschetta M. Unenhanced breast MRI (STIR, T2-weighted TSE, DWIBS): an accurate and alternative strategy for detecting and differentiating breast lesions. Magn Reson Imaging 2015;33:951–5.
47. Le Bihan D, Breton E, Lallemand D, Grenier P, Cabanis E, Laval-Jeantet M. MR imaging of intravoxel incoherent motions: application to diffusion and perfusion in neurologic disorders. Radiology 1986;161:401–7.
48. Sigmund EE, Cho GY, Kim S, Finn M, Moccaldi M, Jensen JH, et al. Intravoxel incoherent motion imaging of tumor microenvironment in locally advanced breast cancer. Magn Reson Med 2011;65:1437–47.
49. Cho GY, Gennaro L, Sutton EJ, Zabor EC, Zhang Z, Giri D, et al. Intravoxel incoherent motion (IVIM) histogram biomarkers for prediction of neoadjuvant treatment response in breast cancer patients. Eur J Radiol Open 2017;4:101–7.
50. Hammond MEH, Hayes DF, Wolff AC, Mangu PB, Temin S. American society of clinical oncology/college of american pathologists guideline recommendations for immunohistochemical testing of estrogen and progesterone receptors in breast cancer. J Oncol Pract 2010;6:195–7.
51. Wolff AC, Hammond MEH, Hicks DG, Dowsett M, McShane LM, Allison KH, et al. Recommendations for human epidermal growth factor receptor 2 testing in breast cancer: American Society of Clinical Oncology/College of American Pathologists Clinical Practice Guideline Update. J Clin Oncol 2013;31:3997–4013.
52. Wolff AC, Hammond MEH, Allison KH, Harvey BE, Mangu PB, Bartlett JMS, et al. Human epidermal growth factor receptor 2 testing in breast cancer: American Society of Clinical Oncology/College of American pathologists clinical practice guideline focused update. J Clin Oncol 2018;36:2105–22.

Downloaded from clincancerres.aacrjournals.org on October 19, 2021. © 2021 American Association for Cancer Research.

Published OnlineFirst November 4, 2020; DOI: 10.1158/1078-0432.CCR-20-2017

AACR American Association for Cancer Research

Clinical Cancer Research

Discrimination of Breast Cancer from Healthy Breast Tissue Using a Three-component Diffusion-weighted MRI Model

Maren M. Sjaastad Andreassen, Ana E. Rodríguez-Soto, Christopher C. Conlin, et al.

Clin Cancer Res 2021;27:1094-1104. Published OnlineFirst November 4, 2020.

Updated version	Access the most recent version of this article at: doi:10.1158/1078-0432.CCR-20-2017
Supplementary Material	Access the most recent supplemental material at: http://clincancerres.aacrjournals.org/content/suppl/2020/11/04/1078-0432.CCR-20-2017.DC1

Cited articles	This article cites 50 articles, 6 of which you can access for free at: http://clincancerres.aacrjournals.org/content/27/4/1094.full#ref-list-1

E-mail alerts	Sign up to receive free email-alerts related to this article or journal.
Reprints and Subscriptions	To order reprints of this article or to subscribe to the journal, contact the AACR Publications Department at pubs@aacr.org.
Permissions	To request permission to re-use all or part of this article, use this link http://clincancerres.aacrjournals.org/content/27/4/1094. Click on "Request Permissions" which will take you to the Copyright Clearance Center's (CCC) Rightslink site.

Downloaded from clincancerres.aacrjournals.org on October 19, 2021. © 2021 American Association for Cancer Research.